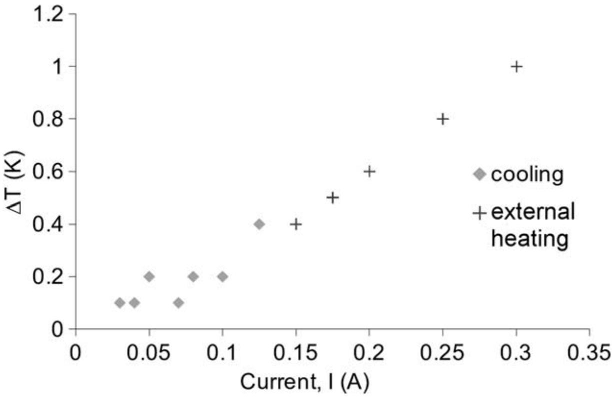


**Figure 2** Microcooler appears to show very good levels of cooling

anode contact. This method will be invaluable for autoprobing across a wafer of microoolers. Equation (1) can be rearranged in the form of $y = mx + c$ (2).

$$\frac{I^2}{\Delta T} = \frac{ST_c}{R} \cdot \frac{I}{\Delta T} - \frac{1}{R\Phi_c} \tag{2}$$

From Eq. (2) the gradient of the plot ($m$) is $\frac{ST_c}{R}$ and should always be positive, as $S$, $T_c$, and $R$ all have positive values.

Equation (2) has been applied to experimental results of two microcoolers. The first microcooler, the DC probes were in direct contact with the cooler contacts and $\Delta T$ was measured as a function of increasing current supplied to the cooler. Figure 2 shows $\Delta T$ increasing with increasing current and $\Delta T$ temperature in excess of 1.2°C for a GaAs based microcooler. However, when the results were plotted using Eq. (2) two gradients were obtained (Fig. 3), the positive gradient representing the range of $\Delta T$ where cooling was taking place at the cathode contact and the negative gradient was attributed to the increase in $\Delta T$ due to heating effects at the anode contact. It is interesting to note that this particular microcooler only gave 0.4°C of actual cooling at the cathode contact, which was in closer agreement with published data on GaAs microcoolers [6].

A second GaAs microcooler fabricated on wafer was arranged with contact pads to keep the DC probes thermally isolated from the microcooler. $\Delta T$ was again measured as a function of the DC current being applied to the microcooler. The microcooler gave the more usual characteristic of Figure 4 $\Delta T$ increasing with current, and then decreasing with current as self-heating at the cathode contact predominated. The results were plotted in Figure 4 using Eq. (2) and this time showing $\Delta T$ is positive when the cathode was cooled ($T_h > T_c$), and when $\Delta T$ was negative when self-heating occurred at the cathode contact ($T_h < T_c$).

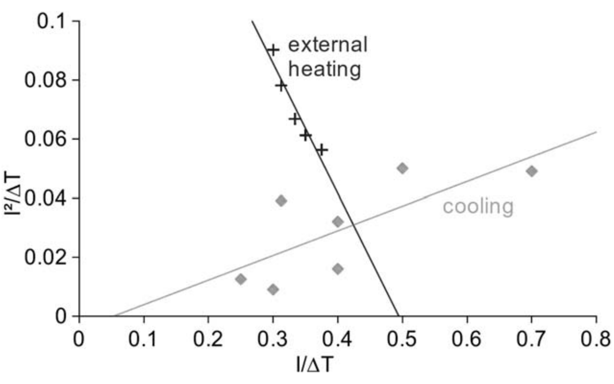


**Figure 3** Results from Figure 2 plotted to (3), showing negative gradient and therefore, external heating effects

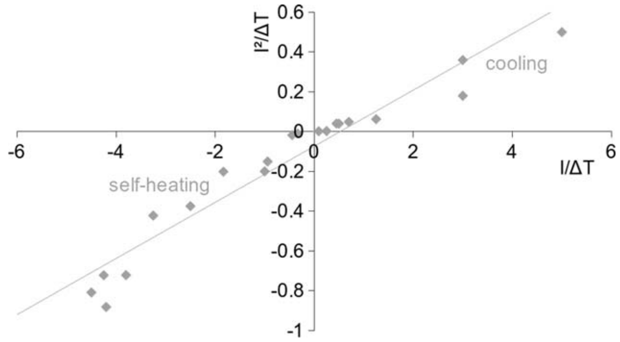


**Figure 4** Thermally isolated cooler, gradient is always positive

## 4. CONCLUSION

The article shows that $\Delta T$ and therefore cooling performance of a microcooler can be misinterpreted, particularly if the microcoolers are fabricated on wafer and DC probed to obtain a map of $\Delta T$ across the wafer. A simple analysis was presented to assist in the interpretation of $\Delta T$ as to whether it was due to cooling of the cathode contact or heating of the anode cathode.

## ACKNOWLEDGMENT

This work was supported by EPSRC through grants EP/H011366/1, EP/H011862/1, EP/H012532/1, and EP/H012966/1.

## REFERENCES

1. R.J. Trew, D.S. Green, and J.B. Shealy, AlGaN/GaN HFET reliability, IEEE Microwave Mag 10 (2009), 116–127.
2. Y. Zhang, G. Zeng, J. Piprek, A. Bar-Cohen, and A. Shakouri, Superlattice microrefrigerators fusion bonded with optoelectronic devices, IEEE Trans Compon Packag Technol 28 (2005), 658–666.
3. C.H. Oxley, R.H. Hopper, D. Prime, M. Leaper, G.A. Evans, and A. Levick, Probe propels IR thermal microscopy to a new level, Compd Semiconduct 17 (2011), 33–36.
4. Y. Zhang, G. Zeng, C. Hoffman, A. Bar-Cohen, and A. Shakouri, Enhanced hot spot cooling using bonded superlattice microcoolers with a trench structure, IEEE Trans Compon Packag Technol 31 (2008), 552–558.
5. A. Shakouri, E.Y. Lee, D.L. Smith, V. Narayanamurti, and J.E. Bowers, Thermoelectric effects in submicron heterostructure barriers, Microscale Thermophys Eng 2 (1998), 37–47.
6. J. Zhang, N.G. Anderson, and K.M. Lau, AlGaAs Superlattice Microcoolers, Appl Phys Lett 83 (2003), 374–376.



# THREE-DIMENSIONAL SUBWAVELENGTH CONFINEMENT OF A PHOTONIC NANOJET USING A PLASMONIC NANOANTENNA GAP

**Mehdi Hasan and Jamesina J. Simpson**
University of Utah, Department of Electrical and Computer Engineering, 50 S. Central Campus Dr., Rm 3280, Salt Lake City, UT 84112; Corresponding author: m.hasan@utah.edu

*Received 2 April 2014*

**ABSTRACT:** *Using 3D finite-difference time-domain modeling, a microsphere-generating nanojet and gold nanoantenna gap are* *optimized to achieve 3D nanojet confinement to a subwavelength volume of about 0.009* μ*m*$^3$ *(wherein the edges of the volume are defined at 1/e*$^2$ *of the maximum electric-field intensity) for an incident wavelength of 633 nm.*  Microwave Opt Technol Lett 56:2700–2706, 2014; View this article online at wileyonlinelibrary.com. DOI 10.1002/mop.28680

**Key words:** *photonic nanojet; plasmonic nanoantenna gap; subwavelength confinement; whispering gallery mode; finite-difference time-domain*

## 1. INTRODUCTION

A 2004 paper [1] reported the existence of a "photonic nanojet," which was discovered using finite-difference time-domain (FDTD) [2] simulations. FDTD-predicted photonic nanojets have since been experimentally observed [3–5]. A photonic nanojet is a subwavelength waist, high-intensity electromagnetic beam capable of propagating multiple wavelengths from the shadow-side surface of an illuminated lossless dielectric microcylinder or microsphere [1, 6, 7]. Photonic nanojets are formed for a wide range of microcylinder / microsphere diameters (from $\sim$ two wavelengths, $\lambda$ to greater than $40\lambda$) if the refractive index contrast relative to the background is less than about 2:1 [7–9]. Photonic nanojets have been proposed for applications ranging from optical data storage [5, 10] to ultramicroscopy [1], high-speed photodetectors [11], enhanced fluorescence correlation spectroscopy [12], localized detection of embedded ultrasubwavelength inhomogeneities [13], and optical lithography [14], and so forth. The photonic nanojets that have been generated and used to date are scientifically interesting and useful for a variety of applications because the transverse beam waist of the nanojet can be made somewhat smaller than the diffraction limit (to $\sim\lambda/3$). However, photonic nanojets generated by plane-wave illumination do not yield three-dimensional (3D) subwavelength light confinement. For plane-wave illumination, the nanojet longitudinal length may extend $\sim 2\lambda$ from the edge of the sphere and even up to $20\lambda$ [13]. It is possible to generate 3D confinement of a photonic nanojet in both longitudinal and transverse directions using a highly specialized source (e.g., a tightly focused Gaussian beam [15]), however, this confinement is only useful under specific circumstances in which there are flexibility to choose and control the source.

We report a new means to confine photonic nanojets in 3D to a subwavelength volume by placing in its path a plasmonic dipole nanoantenna gap (also can be considered as a truncated plasmonic waveguide) [16]. This 3D subwavelength confinement is achieved for plane-wave illumination, thereby providing a new feature for nanojets and opening up new application possibilities, such as high-speed photodetectors [11], nanoscale light sources [17], optical lithography [18], and so forth. Additionally, we find that by placing a subwavelength nanoantenna gaps into the path of the nanojet increases the intensity of the nanojet [19]. Plasmonic dipole nanoantenna gap are known to concentrate electromagnetic energy into a subwavelength volume at the exiting side of the nanoantenna gap for plane-wave illumination [16, 20]. We find here that, a nanoantenna gap can be used to provide 3D subwavelength confinement of a nanojet. This phenomenon is also observed when a whispering gallery mode (WGM) is excited in the microsphere.

3D FDTD modeling is used to demonstrate the 3D subwavelength confinement and enhanced optical energy concentration capability of a photonic nanojet nanoantenna gap light-collection system, both when WGM resonances are and are not excited in the microsphere. We find that for plane-wave illumination of a 3.1 μm ($\sim 5\lambda$) - diameter polystyrene microsphere with a gold nanoantenna gap of transverse dimensions $100 \times 200$ nm$^2$ in its path can yield:

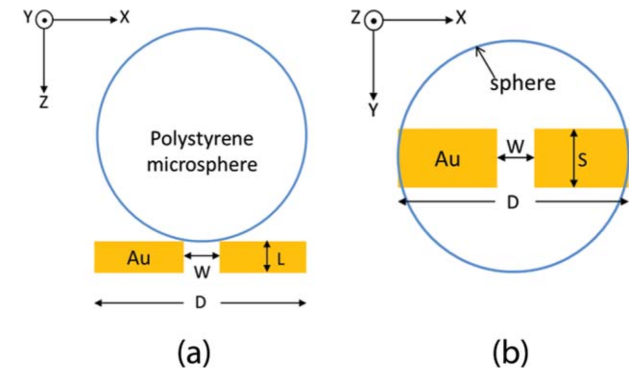


**Figure 1** (a) Side view (not to scale) and (b) top view (not to scale), of the 3D microsphere-generating nanojet and nanoantenna geometry. The microsphere diameter ($D$) is 3.1 μm, $W$ = width of the nanoantenna gap, $S = 2W$, and $L$ = thickness of the nanoantenna. [Color figure can be viewed in the online issue, which is available at wileyonlinelibrary.com]

- A 3D confinement of the nanojet in to a subwavelength volume of about 0.009 μm$^3$ (wherein the edges of the volume are defined at $1/e^2$ of the maximum electric ($E$)-field intensity) for an incident $\lambda = 633$ nm.
- A doubling of the electric field magnitude in the gap region and just beyond the nanoantenna gap, compared to the nanojet-only case (no nanoantenna gap included).
- An absorption enhancement factor of nearly 200 in a subwavelength volume of about 0.002 μm$^3$ just behind the exiting end of the gold nanoantenna gap.
- Enhanced, 3D subwavelength concentration of light for both resonant and nonresonant plasmonic nanoantenna gaps.
- A 3D confinement of the nanojet in to a subwavelength volume of about 0.01 μm$^3$ when the WGM at an incident wavelength $\lambda = 786.95$ nm is excited (which is not far from the incident wavelength of 633 nm).

We note that the works of Refs. [21] and [22] involved placing a nanoaperture into the path of a nanojet. However, the studies performed in those papers are two-dimensional and they do not cover the 3D nanojet confinement capabilities of the nanojet+nanoantenna gap system.

## 2. GENERAL GEOMETRY

Figure 1 illustrates the device geometry (not to scale). The overlying microsphere is comprised of polystyrene (refractive index, $n = 1.59$) and is of diameter ($D = 5\lambda$) 3.1 μm. The dipole nanoantenna gap has an area of $W \times S$ nm$^2$ in the $x$-$y$ plane, respectively, with $S = 2W$; the antenna length $D = 3.1$ μm. $W = 100$ nm $\approx \lambda/6$ is chosen to obtain a tight confinement of modes through the nanoantenna gap. It is illuminated from the top (+$z$-direction) by an $x$-polarized plane wave.

The geometry of Figure 1 yields a light-collection system that first uses a polystyrene dielectric microsphere to form a nanojet somewhat smaller than the diffraction limit in the transverse directions ($x$- and $y$-directions), and then uses a subwavelength nanoantenna gap to: (1) further confine the nanojet to ultrasubwavelength dimensions in the transverse directions; and (2) confine the nanojet to a subwavelength dimension in the longitudinal direction. For all simulation cases, the incident

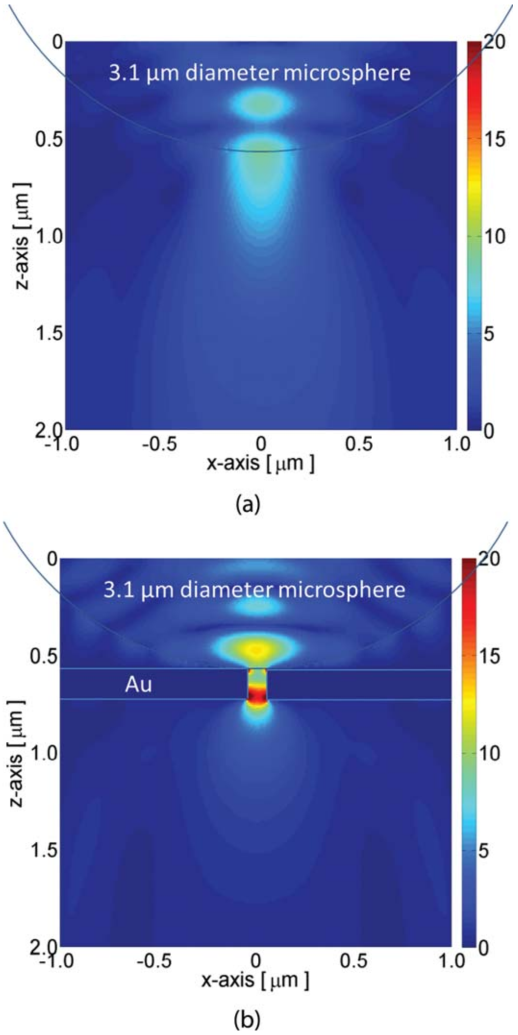


**Figure 2** Visualization of the FDTD-computed scattered E-field (|$E$|) for (a) a nanojet generated by a 3.1 μm diameter polystyrene microsphere in air and (b) a compressed nanojet generated by a 3.1 μm diameter polystyrene microsphere with a resonant gold nanoantenna gap (centered within the path of the nanojet and having $W = 100$ nm, $S = 200$ nm, and $L = 150$ nm), for an incident $\lambda = 633$ nm. [Color figure can be viewed in the online issue, which is available at wileyonlinelibrary.com]

wavelength is $\lambda = 633$ nm when the nanojet induced mode (NIM) is excited and $\lambda = 786.95$ nm when the WGM is excited in the microsphere. The gold is modeled using a Lorentz–Drude model [2, 23], for which the parameters are taken from Ref. [23]. A uniform cubic grid cell size of 10 nm is used and the entire modeling space spans $6 \times 6 \times 6$ $\mu m^3$. A time step set to the Courant limit is used as well as a convolutional perfectly matched layer (CPML) for the absorbing boundary condition [24] and all the results are generated after sufficient time steps to ensure steady state condition.

### 3. OPTIMIZED 3D SUBWAVELENGTH CONFINEMENT OF A PHOTONIC NANOJET

In this Section, the homogeneous polystyrene microsphere is modeled in air by itself in the FDTD grid for an incident $\lambda = 633$ nm. The resulting nanojet generated by the microsphere is shown in Figure 2(a). Note that the microsphere (size and composition) has been designed to provide a nanojet focal point immediately adjacent to the sphere surface [9]. Focusing the

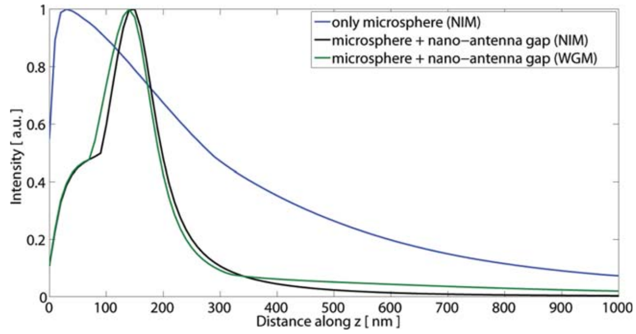


**Figure 3** FDTD-computed intensity (normalized to the respective maximum) versus distance along the $z$-axis from the microsphere's shadow-side surface (along the center axis of the nanojet and the nanoantenna gap) for the case of a NIM-excited microsphere with a plasmonic nanoantenna gap ($W = 100$ nm, $S = 200$ nm, and $L = 150$ nm), a WGM-excited microsphere with a plasmonic nanoantenna gap of the same dimensions, and a NIM-excited microsphere only. [Color figure can be viewed in the online issue, which is available at wileyonlinelibrary.com]

nanojet at the sphere surface will yield the smallest possible subwavelength 3D confinement when the nanoantenna gap is placed in its path. Note that the nanojet of Figure 2(a) is visually not very pronounced. This is because a colorbar scale of 0–20 (V/m) is used in Figure 2(a) so that it may be directly compared with the results of Figure 2(b). In Figure 2(b), the plasmonic nanoantenna gap is introduced into the path of the nanojet of Figure 2(a). Comparing Figures 2(a) and 2(b), we see that the nanoantenna gap more than doubles the enhancement for the scattered E-field (|$E$|) in the gap region and just beyond (below) the aperture. Further, the nanojet is confined in all three Cartesian directions by the nanoantenna gap to a highly

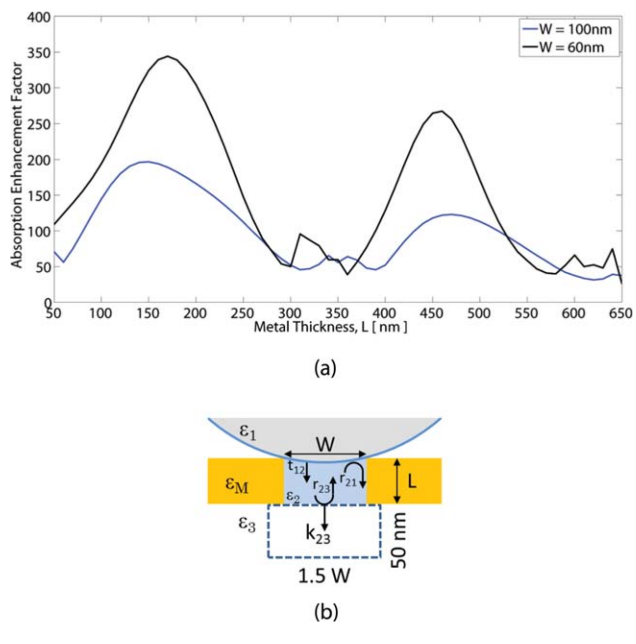


**Figure 4** (a) Plot of the absorption enhancement factor in a nanoscale volume directly beneath the nanoantenna gap as a function of the antenna thickness for two different nanoantenna gap widths ($W = 100$ and 60 nm) for an incident $\lambda = 633$ nm. These FDTD simulated results show agreement with the Fabry–Perot model [20]. (b) Schematic showing the relevant scattering coefficients used for the model. [Color figure can be viewed in the online issue, which is available at wileyonlinelibrary.com]

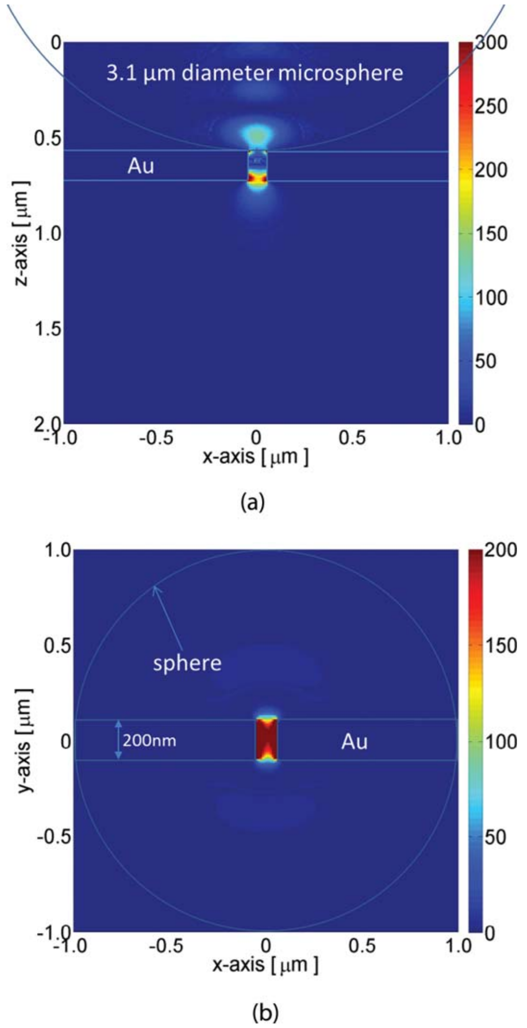


**Figure 5** FDTD-calculated optical near-field intensity ($|E|^2$): (a) in the $x$-$z$ plane for a resonant plasmonic nanoantenna gap with the nanojet producing microsphere; and (b) same as (a) but in the $x$-$y$ plane 10 nm beneath the nanoantenna gap. For both cases, $W = 100$ nm, $S = 200$ nm, $L = 150$ nm, and an incident $\lambda = 633$ nm. [Color figure can be viewed in the online issue, which is available at wileyonlinelibrary.com]

subwavelength dimension. The subwavelength confinement in the $z$-direction (longitudinal direction) will be quantified below using the results of Figure 3. The transverse ($x$- and $y$-direction) subwavelength confinement of the nanojet+nanoantenna gap system will be further quantified in Section 4 using the results of Figure 6.

Figure 3 plots the normalized intensity versus distance from the microsphere along the center axis of the nanojet in the $z$-direction. It is apparent from Figure 3 that the presence of the nanoantenna gap shifts the focus point of the nanojet from the surface of the microsphere to the exiting edge of the nanoantenna gap (the maximum intensity is shifted from $z = 30$ to 150 nm, when the nanoantenna gap is introduced). Further, we can now begin to quantify the subwavelength confinement of the nanojet due to the nanoantenna gap. We will define the longitudinal ($z$-direction) waist of the confined nanojet to be between $1/e^2$ of the maximum value and will be denoted by $W_z$. $W_z$ is determined to be ~280 nm for the microsphere+nanoantenna gap NIM case (incident $\lambda = 633$ nm) and similarly it is ~270 nm for the microsphere+nanoantenna gap WGM case (incident $\lambda = 786.95$ nm). We believe these are the smallest longitudinal dimensions achieved to date in the scientific literature for photonic nanojets by a factor of at least four. For the microsphere-only NIM case $W_z$ is much larger, at approximately 800 nm.

## 4. ENHANCED OPTICAL ENERGY CONCENTRATION IN A SUBWAVELENGTH VOLUME

Next, we analyze a photonic nanojet illuminating either resonant or nonresonant nanoantenna gaps [16, 17, 20]. We will use 3D FDTD to quantify the absorption enhancement factor in a nanoscale volume of $1.5W \times 1.5S \times 50$ nm$^3$ just beneath the nanoantenna gap, where $W$ is the width of the nanoantenna gap (100 and 60 nm) and $S = 2W$. Figure 4(a) shows the absorption enhancement factor plotted as the energy in a subwavelength volume just below the exiting end of the nanoantenna gap as a function of nanoantenna thickness for two different gap widths. Both curves are normalized to the energy in the same volume without the microsphere and the nanoantenna, which yields an absorption enhancement factor of nearly 200 for $L \approx 150$ nm, $W = 100$ nm, and $S = 200$ nm in a subwavelength volume of about 0.002 μm$^3$. The length dependence of the absorption enhancement factor is quite similar to optical transmission, which is described with a Fabry–Perot resonator model [20]. The fundamental scattering coefficients of the metal-dielectric-metal (MDM) system are shown in Figure 4(b). The analytic equation for the absorption in the subwavelength region is given by,

Absorption$=\frac{k_{23}|t_{12}|^2 e^{-2|k''_{MDM}|L}}{|1-r_{21}r_{23}e^{2ik_{\mathrm{MDM}}L}|^2}$, where $k_{\mathrm{MDM}} = k'_{\mathrm{MDM}} + ik''_{\mathrm{MDM}}$ is the complex wave vector of the gap plasmon mode, $t$ is

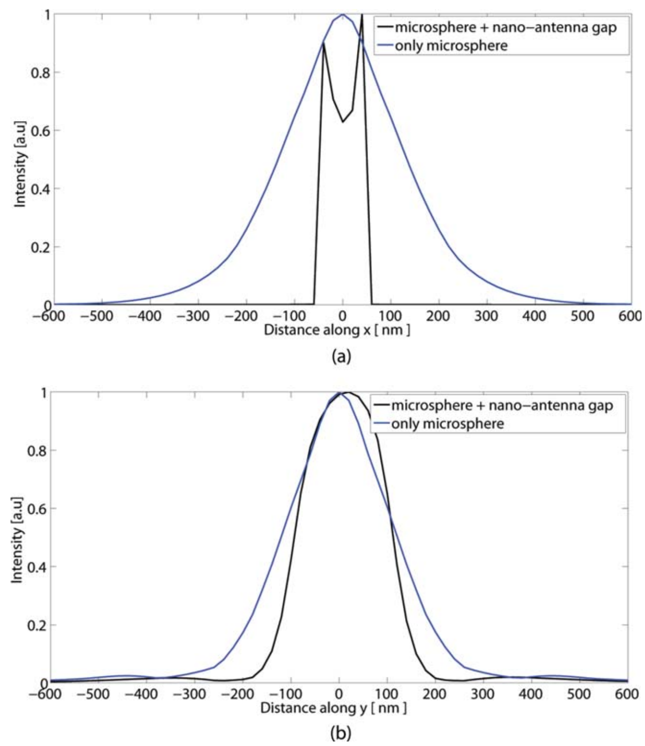


**Figure 6** Intensity (normalized to the respective maximum) variation (a) at the center of the grid in the $y$-direction and plotted along the $x$-axis at a depth of 10 nm (in the $z$-direction) below the nanoantenna gap, compared to the intensity variation for the case of only a microsphere (no nanoantenna gap) at the focus point (maximum intensity, 30 nm from the sphere surface) and (b) same as (a) but at the center of the grid in the $x$-direction and plotted along the $y$-axis; an incident $\lambda = 633$ nm. [Color figure can be viewed in the online issue, which is available at wileyonlinelibrary.com]

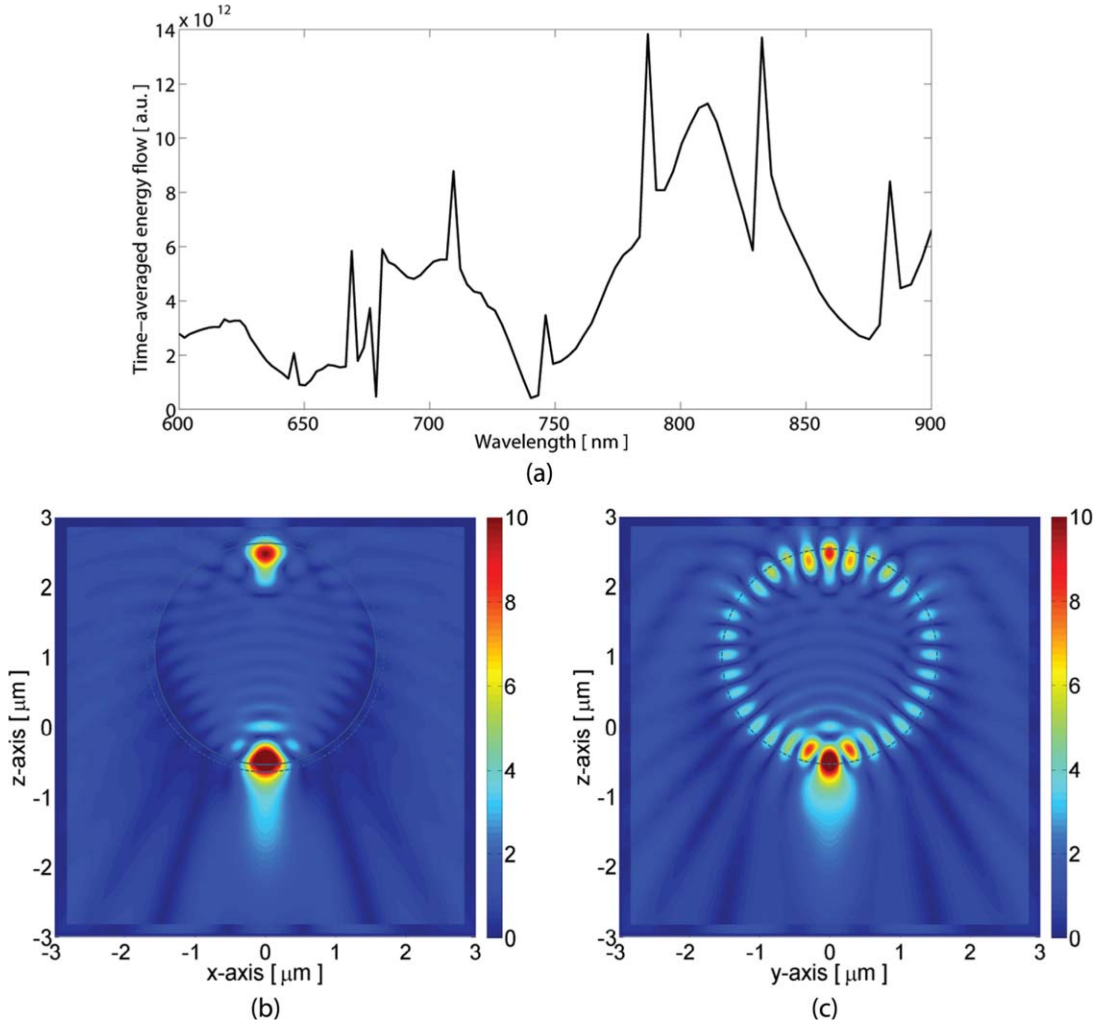


**Figure 7** (a) FDTD-calculated time-averaged energy flow, averaged over the area $A = \pi\ (3150^2 - 3100^2)\ \text{nm}^2 = 981747.7\ \text{nm}^2$ of an annulus surrounding the microsphere [see the two concentric circles in Fig. 7(b)] versus wavelength. Visualization of the FDTD-computed scattered E-field ($|E|$) for a 3.1 μm diameter polystyrene microsphere when a WGM is excited at an incident wavelength $\lambda = 786.95$ nm for (b) *x*-*z* plane, and (c) *y*-*z* plane. [Color figure can be viewed in the online issue, which is available at wileyonlinelibrary.com]

transmission coefficient, and $r$ is reflection coefficient [20]. The curves of Figure 4(a) show agreement with the above Fabry–Perot model absorption equation. From Figure 4(a), we see there is almost a width independent location of first-order resonance at $L \approx 150$ nm for $W = 100$ nm and at $L \approx 160$ nm for $W = 60$ nm. There is strong resonant enhancement for $L = 150$ nm and $W = 100$ nm, and there is also strong nonresonant enhancement for $L = 100$ nm and $W = 100$ nm. Also, from these absorption enhancement factor results, we observe that both resonant and nonresonant nanoantenna gaps yield substantial energy enhancement when illuminated by a photonic nanojet.

Next, we examine cross-sectional results of the optical intensity for a resonant plasmonic nanoantenna gap with the nanojet producing microsphere. Figures 5(a) and 5(b), show significantly higher enhancement when a nanojet is used to illuminate the same nanoantenna gap. In Figure 5(b), the lightning-rod effect [16] is clear for the resonant nanoantenna gap case. In Figure 5(b), the maximum intensity is seen to be concentrated approximately over a subwavelength focus spot of area $100 \times 200\ \text{nm}^2$ in the *x*-*y* plane 10 nm below the nanoantenna gap. Figure 6(a) shows the intensity variation at the center of the grid in the *y*-direction along the transverse (*x*-) axis at a depth of 10 nm below the nanoantenna gap (in the *z*-direction) for a microsphere+nanoantenna gap case (i.e., $W = 100$ nm, $S = 200$ nm, and $L = 150$ nm). For comparison, the intensity variation provided by only a microsphere at its focus point (maximum intensity, 30 nm from the sphere surface) is shown for when the NIM is excited ($\lambda = 633$ nm). The transverse waist along the *x*-axis is defined as being between the $1/e^2$ of the maximum value and is denoted by $W_x$. $W_x$ for the microsphere-only case is about 480 nm, whereas $W_x$ is much smaller at 120 nm, for the microsphere+nanoantenna gap NIM case. Figure 6(b) then shows the intensity variation at the center of the grid in the *x*-directions along the transverse (*y*-) axis at a depth of 10 nm below the nanoantenna gap (in the *z*-direction) for a microsphere+nanoantenna gap case (i.e., $W = 100$ nm, $S = 200$ nm, and $L = 150$ nm). For comparison, the intensity variation provided by only a microsphere at its focus point (maximum intensity, 30 nm from the sphere surface) is shown for when the NIM is excited ($\lambda = 633$ nm). The transverse waist along the *y*-axis defined at $1/e^2$ of the maximum value and is denoted by $W_y$. $W_y$ for the microsphere-only case is about 420 nm, and for the microsphere+nanoantenna gap case $W_y$ is

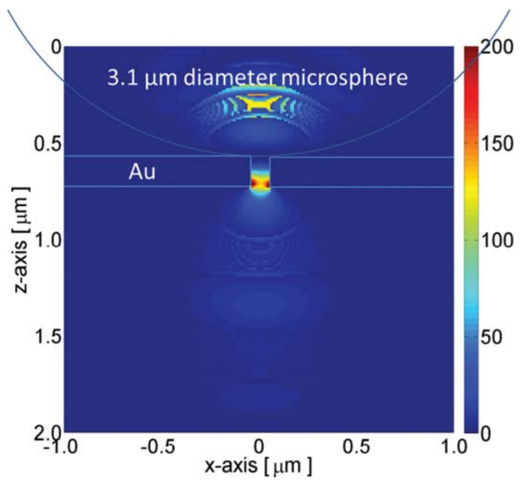


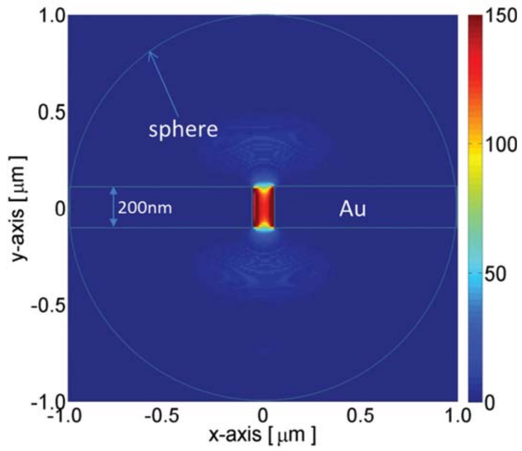


**Figure 8** FDTD-calculated optical near-field intensity ($|E|^2$): (a) in the $x$-$z$ plane for a plasmonic nanoantenna gap with a microsphere (when the WGM is excited); (b) same as (a) but in the $x$-$y$ plane 10 nm beneath the nanoantenna gap. For both cases, $W = 100$ nm, $S = 200$ nm, $L = 150$ nm, and an incident $\lambda = 786.95$ nm. [Color figure can be viewed in the online issue, which is available at wileyonlinelibrary.com]

about 280 nm. Thus, using the results of Figure 6 along with the results of Figure 3, the photonic nanojet is confined to a subwavelength volume defined by $W_x \times W_y \times W_z = 0.12 \times 0.28 \times 0.28$ $\mu m^3$, which is equal to about 0.009 $\mu m^3$.

## 5. WGM EFFECT ON OPTICAL ENERGY CONCENTRATION AND SUBWAVELENGTH CONFINEMENT

The WGM affects the focus properties, for example, field enhancement and full width at half maximum, of a microsphere [25]. The time-averaged energy flow spectrum of the 3.1 μm polystyrene microsphere averaged near the microsphere surface [i.e., the annulus of Fig. 7(b)] is shown in Figure 7(a) [21, 22]. A strong WGM appears at an incident $\lambda = 786.95$ nm. Details of the distribution of the electric field at $\lambda = 786.95$ nm in the $x$-$z$ plane and $y$-$z$ plane is presented in Figures 7(b) and 7(c), respectively. Note that the nanojet focus is now slightly inside the microsphere relative to the case when the WGM is not excited (in which case it is focused more just outside the surface as seen in Fig. 2). Using the results of Figure 7, cross-sectional results are examined for the optical intensity of a microsphere+nanoantenna gap system when a strong WGM is excited in the microsphere at the incident $\lambda = 786.95$ nm. Figures 8(a) and 8(b) still show significant enhancement when a WGM is excited in the microsphere to illuminate a nanoantenna gap relative to Figure 5 [note the change in the colorbar scale used in Figs. 5(a) and 5(b) vs. Figs. 8(a) and 8(b)]. In Figure 8(a), a reduction in maximum intensity is seen compared to Figure 5(a) because the nanoantenna gap does not yield maximum enhancement at $\lambda = 786.95$ nm. This is due to the fact that the nanoantenna gap dimensions are not optimized for an incident $\lambda = 786.95$ nm. In Figure 8(b), the maximum intensity is concentrated approximately over a transverse focus spot of area $100 \times 200$ nm$^2$ in the $x$-$y$ plane 10 nm below the nanoantenna gap, similar to Figure 5(c).

Figure 9(a) shows the intensity variation at the center of the grid in the y direction along the transverse ($x$-) axis at a depth of 10 nm below the nanoantenna gap (in the $z$-direction) for a microsphere+nanoantenna gap case (i.e., $W = 100$ nm, $S = 200$ nm, and $L = 150$ nm). For comparison, the intensity variation provided by only a microsphere near its focus point (maximum intensity, 10 nm from the sphere surface) is shown for when the WGM is excited ($\lambda = 786.95$ nm). $W_x$ for the microsphere-only case is about 500 nm, whereas $W_x$ for the microsphere+nanoantenna gap is 120 nm. Figure 9(b) shows the intensity variation at the center of the grid in the $x$-direction along the transverse ($y$-) axis at a depth of 10 nm below the nanoantenna gap (in the $z$-direction) for a

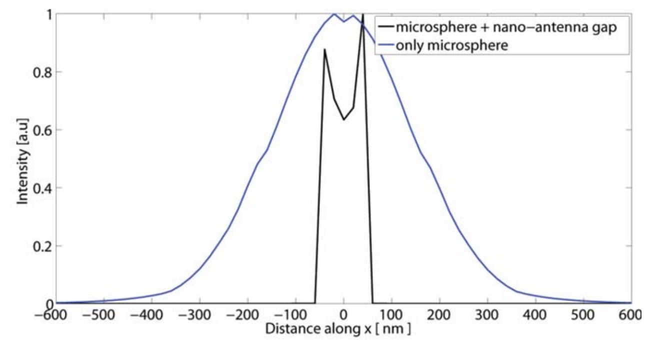


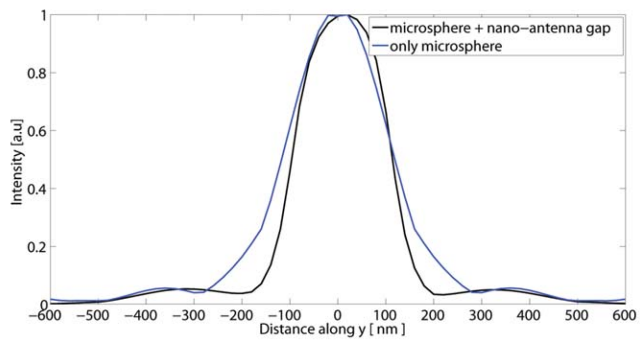


**Figure 9** Intensity (normalized to the respective maximum) variation (a) at the center of the grid in the $y$-direction and plotted along the $x$-axis at a depth of 10 nm (in the $z$-direction) below the nanoantenna gap, compared to the intensity variation for the case of only a microsphere (no nanoantenna) at the focus point (maximum intensity, 10 nm from the sphere surface) and (b) same as (a) but at the center of the grid in the $x$-direction and plotted along the $y$-axis; an incident $\lambda = 786.95$ nm. [Color figure can be viewed in the online issue, which is available at wileyonlinelibrary.com]

microsphere+nanoantenna gap case (i.e., $W = 100$ nm, $S = 200$ nm, and $L = 150$ nm). For comparison, the intensity variation provided by only a microsphere near its focus point (maximum intensity, 10 nm from the sphere surface) is shown for when the WGM is excited ($\lambda = 786.95$ nm). $W_y$ for the microsphere-only case is about 420 nm, and $W_y$ for the microsphere+nanoantenna gap case is about 310 nm. Using also the results of Figure 3, the nanojet is confined in a subwavelength volume defined by $W_x \times W_y \times W_z = 0.12 \times 0.31 \times 0.27$ $\mu m^3$, which is equal to about 0.01 $\mu m^3$, just slightly larger than the NIM results of Section 4.

## CONCLUSION

In conclusion, a new means of achieving 3D light confinement for a photonic nanojet has been demonstrated by placing a plasmonic dipole nanoantenna gap in its path. 3D FDTD results illustrated that a gold nanoantenna gap of width 100 nm, length 200 nm, and thickness 150 nm confines a nanojet generated by a polystyrene microsphere of diameter 3.1 μm ($5\lambda$) to a subwavelngth volume of about 0.009 $\mu m^3$ for, an incident $\lambda = 633$ nm. An absorption enhancement factor of nearly 200 can be achieved in a subwavelength volume of about 0.002 $\mu m^3$ behind a gold nanoantenna gap when illuminated by the nanojet+nanoantenna gap system. Enhanced concentration of light in a subwavelength volume is achieved for both resonant and nonresonant plasmonic nanoantenna gaps. 3D FDTD results also demonstrated that a gold nanoantenna gap of width 100 nm, length 200 nm, and thickness 150 nm confines the nanojet to a subwavelngth volume of about 0.01 $\mu m^3$ when the WGM is excited at an incident $\lambda = 786.95$ nm. These results may find utility in applications, such as high-speed photodetectors, nanoscale light sources, optical lithography, and so forth.

## ACKNOWLEDGMENT

The authors acknowledge the University of Utah, Center for High Performance Computing (CHPC) for providing supercomputing resources.

## REFERENCES

1. Z. Chen, A. Taflove, and V. Backman, Photonic nanojet enhancement of backscattering of light by nanoparticles: A potential novel visible-light ultramicroscopy technique, Opt Express 12 (2004), 1214–1220.
2. A. Taflove and S.C. Hagness, Computational electrodynamics: The finite-difference time-domain method, 3rd ed., Artech, Boston, MA, 2005.
3. P. Ferrand, J. Wenger, A. Devilez, M. Pianta, B. Stout, N. Bonod, E. Popov, and H. Rigneault, Direct imaging of photonic nanojets, Opt Express 16 (2008), 6930–6940.
4. M. Kim, T. Scharf, S. Mühlig, C. Rockstuhl, and H.P. Herzig, Engineering photonic nanojets, Opt Express 19 (2011), 10206–10220.
5. S.C. Kong, A. Sahakian, A. Heifetz, A. Taflove, and V. Backman, Robust detection of deeply subwavelength pits in simulated optical data-storage disks using photonic nanojets, Appl Phys Lett 92 (2008), 21102-1-3.
6. X. Li, Z. Chen, A. Taflove, and V. Backman, Optical analysis of nanoparticles via enhanced backscattering facilitated by 3-D photonic nanojets, Opt Express 13 (2005), 526–533.
7. S. Kong, A. Taflove, and V. Backman, Quasi one-dimensional light beam generated by a graded-index micro-sphere, Opt Express 17 (2009), 3722–3731.
8. A. Heifetz, S.C. Kong, A.V. Sahakian, A. Taflove, and V. Backman, Photonic nanojets, J Comput Theor Nanosci 6 (2009), 1979–1992.
9. S. Lecler, Y. Takakura, and P. Meyrueis, Properties of a three-dimensional photonic jet, Opt Lett 30 (2005), 2641–2643.
10. S.C. Kong, A. Sahakian, A. Taflove, and V. Backman, Photonic nanojet-enabled optical data storage, Opt Express 16 (2008), 13713–13719.
11. M. Hasan and J.J. Simpson, Photonic nanojet-enhanced nanometer-scale germanium photodiode, Appl Opt 52 (2013), 5420–5425.
12. J. Wenger, D. Gérard, H. Aouani, and H. Rigneault, Disposable microscope objective lenses for fluorescence correlation spectroscopy using latex microsphere, Anal Chem 80 (2008), 6800–6804.
13. C. Mendez-Ruiz and J.J. Simpson, Detection of embedded ultra-subwavelength-thin dielectric features using elongated photonic nanojets, Opt Express 18 (2010), 16805–16812.
14. W. Wu, A. Katsnelson, O.G. Memis, and H. Mohseni, A deep sub-wavelength process for the formation of highly uniform arrays of nanoholes and nanopillars, Nanotechnology 18 (2007), 485302-1-4.
15. A. Devilez, N. Bonod, J. Wenger, D. Gérard, B. Stout, H. Rigneault, and E. Popov, Three-dimensional subwavelength confinement of light with dielectric microspheres, Opt Express 17 (2009), 2089–2094.
16. J.A. Schuller, E.S. Barnard, W. Cai, Y.C. Jun, J.S. White, and M.L. Brongersma, Plasmonics for extreme light concentration and manipulation, Nat Mater 9 (2010), 193–204.
17. Y.C. Jun, R.D. Kekatpure, J.S. White, and M.L. Brongersma, Nonresonant enhancement of spontaneous emission in metal-dielectric-metal plasmon waveguide structures, Phys Rev B 78 (2008), 153111-1-4.
18. L. Wang and X. Xu, Numerical study of optical nanolithography using nanoscale bow-tie shaped nano-apertures, J Microsc 229 (2007), 483–489.
19. A. Devilez, B. Strout, and N. Bonod, Compact metallo-dielectric optical antenna for ultra-directional and enhanced radiative emission, ACS Nano 4 (2010), 3390–3396.
20. J.S. White, G. Veronis, Z. Yu, E.S. Barnard, A. Chandran, S. Fan, and M.L. Brongersma, Extraordinary optical absorption through sub-wavelength slits, Opt Lett 34 (2009), 686–688.
21. F.J. Valdivia-Valero and M. Nieto-Vesperinas, Enhanced transmission through subwavelength apertures by excitation of particle localized plasmons and nanojets, Opt Express 19 (2011), 11545–111554.
22. F.J. Valdivia-Valero and M. Nieto-Vesperinas, Optical forces on cylinders near subwavelength slits illuminated by a photonic nanojet, Opt Commun 294 (2013), 351–360.
23. A.D. Rakic, A.B. Djurišic, J.M. Elazar, and M.L. Majewski, Optical properties of metallic films for vertical-cavity optoelectronic devices, Appl Opt 37 (1998), 5271–5283.
24. J.A. Roden and S.D. Gedney, Convolutional PML (CPML): An efficient FDTD implementation of the CFS- PML for arbitrary media, Microwave Opt Technol Lett 27 (2000), 334–339.
25. Y. Duan, G. Barbastathis, and B. Zhang, Classical imaging theory of a microlens with super-resolution, Opt Lett 38 (2013), 2988–2990.



# ANALYSIS OF OPTICAL BEAT INTERFERENCE NOISE SUPPRESSION USING RF-CLIPPING TONE IN OFDMA-PON UPLINK TRANSMISSION

**Seung-Min Yang[1], Kyoung-Hak Mun[1], Chang-hun Kim[1], Sun-Young Jung[1], Sang-Min Jung[1], Seung-Hyun Cho[2], and Sang-Kook Han[1]**
[1] Department of Electrical and Engineering, Yonsei University, Shinchon-Dong, Seodaemoom-Ku, Seoul, 120–749, Korea; Corresponding author: yajamma@naver.com
[2] Electronics and Telecommunications Research Institute (ETRI), 218 Gajeong-ro, Yuseong-gu, Daejeon, 305–700, Korea

*Received 2 April 2014*

**ABSTRACT:** *In orthogonal frequency division multiple access-passive optical network (OFDMA-PON) uplink transmission with a direct detection system, the optical beat interference (OBI) noise is a very critical*